



# CuInS<sub>2</sub> sensitized TiO<sub>2</sub> hybrid nanofibers for improved photocatalytic CO<sub>2</sub> reduction

Feiyan Xu<sup>a</sup>, Jianjun Zhang<sup>a</sup>, Bicheng Zhu<sup>a</sup>, Jiaguo Yu<sup>a,b,\*,</sup>, Jingsan Xu<sup>c,\*</sup>

<sup>a</sup> State Key Laboratory of Advanced Technology for Material Synthesis and Processing, Wuhan University of Technology, Luoshi Road 122, Wuhan, 430070, PR China

<sup>b</sup> Department of Physics, Faculty of Science, King Abdulaziz University, Jeddah, 21589, Saudi Arabia

<sup>c</sup> School of Chemistry, Physics and Mechanical Engineering, Queensland University of Technology, Brisbane, Queensland, 4000, Australia



## ARTICLE INFO

### Keywords:

TiO<sub>2</sub> Nanofiber  
CuInS<sub>2</sub> nanoplates  
Direct Z-scheme heterojunction  
Photocatalytic CO<sub>2</sub> reduction

## ABSTRACT

Photocatalytic CO<sub>2</sub> reduction into solar fuels over photocatalysts has theoretically and practically become a hot research topic. Herein, we fabricated a novel hybrid TiO<sub>2</sub> nanofiber coated by CuInS<sub>2</sub> nanoplates through a hydrothermal method. The materials were characterized by X-ray diffraction, electron microscopes, UV-vis absorption spectra, nitrogen sorption, X-ray photoelectron spectroscopy and electrochemical impedance spectroscopy. The resulting TiO<sub>2</sub>/CuInS<sub>2</sub> hybrid nanofibers exhibit superior photocatalytic activity for CO<sub>2</sub> reduction under irradiation, due to the generation of direct Z-scheme heterojunction between TiO<sub>2</sub> and CuInS<sub>2</sub>. This work may provide an alternate methodology to design and fabricate multicomponent TiO<sub>2</sub>-based photocatalyst for high-efficiency CO<sub>2</sub> photoreduction.

## 1. Introduction

Photocatalytic CO<sub>2</sub> reduction over well-designed catalysts has been considered an emerging way for recycling CO<sub>2</sub> back to renewable fuels, *e.g.*, CH<sub>4</sub> and CH<sub>3</sub>OH with the aid of solar energy, which is regarded as one of the most promising strategies to overcome the energy and environmental crises [1–7]. For example, metal-organic frameworks (MOF), a type of micro-mesoporous hybrid materials, are recently emerging as a new category of materials for CO<sub>2</sub> photo-reduction due to their special structural characteristics and remarkable adsorption capability for CO<sub>2</sub> [8–10]. Besides, TiO<sub>2</sub> as a typical semiconductor photocatalyst, has been frequently studied for CO<sub>2</sub> reduction due to its high stability, nontoxicity and abundant availability [11–14]. However, TiO<sub>2</sub> can only absorb UV-light because of its large band gap [15,16]. Moreover, it shows a fast recombination of the photogenerated electron-hole pairs, which leads to low photocatalytic performance [17–19]. Several approaches have been explored to improve the photocatalytic activities of TiO<sub>2</sub>, including noble metal deposition (*e.g.* Pt, Au, Pd, Ag) [20–24], nonmetal doping (*e.g.* N, C) [25–28], surface sensitization [29,30], coupling with narrow-bandgap semiconductors (*e.g.* CdS, g-C<sub>3</sub>N<sub>4</sub>, Cu<sub>2</sub>O) [31–36] and so on. Among these, hybridizing TiO<sub>2</sub> with other semiconductors is believed to be an effective method to broaden the light absorption and meanwhile improve the separation

and extraction of the photogenerated carriers.

Differing from TiO<sub>2</sub>, CuInS<sub>2</sub> has a narrow direct band gap of 1.50 eV, close to the optimal band gap (1.45 eV) for solar light harvesting [37–39], and meanwhile shows an ultrahigh absorption coefficient ( $1 \times 10^5 \text{ cm}^{-1}$ ). Besides, CuInS<sub>2</sub> shows a pronounced defect tolerance and exceptional radiation hardness as compared to other semiconductors [40–42]. CuInS<sub>2</sub> does not contain any toxic heavy metals and has been investigated for photovoltaics [43], bioimaging [44], and photocatalytic water splitting [45]. For instance, Kudo and coworkers have prepared a ZnS-CuInS<sub>2</sub>-AgInS<sub>2</sub> ternary solid solution which exhibited 7.4% quantum yield of hydrogen production under 520 nm irradiation [45]. In addition, CuInS<sub>2</sub> has been combined with other semiconductors to make composite photocatalysts, such as MoS<sub>2</sub>/CuInS<sub>2</sub> [46], g-C<sub>3</sub>N<sub>4</sub>/CuInS<sub>2</sub> [47], Bi<sub>2</sub>WO<sub>6</sub>/CuInS<sub>2</sub> [48] and ZnO/CuInS<sub>2</sub> [49,50], for enhanced H<sub>2</sub> generation from water splitting or organic pollutants degradation. In these cases, CuInS<sub>2</sub> was presented as nanosheets or quantum dots. It is also reported that CuInS<sub>2</sub> thin films can function as cathodes for photoelectrochemical reduction of CO<sub>2</sub> [51]. However, CuInS<sub>2</sub> involved photocatalysts for direct CO<sub>2</sub> reduction have been rarely demonstrated and more efforts are required to improve the solar driven CO<sub>2</sub>-to-fuel conversion efficiency.

Herein, we report the facile synthesis of TiO<sub>2</sub> nanofibers sensitized with CuInS<sub>2</sub> nanoplates through an *in-situ* hydrothermal process. The

\* Corresponding author.

\*\* Corresponding author at: State Key Laboratory of Advanced Technology for Material Synthesis and Processing, Wuhan University of Technology, Luoshi Road 122, Wuhan, 430070, PR China.

E-mail addresses: [jiaguoyu@yahoo.com](mailto:jiaguoyu@yahoo.com) (J. Yu), [jingsan.xu@qut.edu.au](mailto:jingsan.xu@qut.edu.au) (J. Xu).

obtained  $\text{TiO}_2/\text{CuInS}_2$  hybrid nanofibers show increased optical absorption and enhanced charge separation, and thus improved photocatalytic  $\text{CO}_2$  reduction was achieved. Based on the experimental data and DFT calculation, we propose a direct Z-scheme heterojunction formed between the  $\text{TiO}_2$  nanofiber and the  $\text{CuInS}_2$  nanoplates.

## 2. Experimental details

### 2.1. Materials and synthesis of electrospun $\text{TiO}_2$ nanofibers

Poly(vinyl pyrrolidone) with an average molecular weight of 1,300,000 was purchased from Tianjin Bodi Chemical Co., Ltd. The other chemicals were of analytical grade and purchased from Shanghai Chemical Company. Electrospun  $\text{TiO}_2$  nanofibers were prepared according to our previous work [11]. Typically, 2.0 g of Tetraethyl titinate (TBT) and 0.75 g of PVP were dissolved in the solvent containing 10.0 g of ethanol and 2.0 g of acetic acid. The mixture became a transparent light yellow solution after magnetically stirring for 5 h at room temperature. The solution was then poured into a 10 mL syringe in the electrospinning setup. The steel needle had a distance of 10 cm and a voltage of 15 kV with respect to the static collector. And the solution feeding rate is maintained at 2.5 mL h<sup>-1</sup>. The collected electrospun samples ( $\text{TiO}_2$  precursors) were calcined at 550 °C in air for 2 h with a ramping rate of 2 °C min<sup>-1</sup>.

### 2.2. Preparation of $\text{TiO}_2/\text{CuInS}_2$ heterostructures

$\text{TiO}_2$  nanofibers were first chemically etched to increase surface roughness. Briefly,  $\text{TiO}_2$  nanofiber was immersed in a concentrated NaOH solution (10 M) at 160 °C for 15 min, and washed with dilute HCl solution and water for several times. As-etched  $\text{TiO}_2$  fibers were then annealed at 450 °C in air for 1 h with a ramping rate of 2 °C min<sup>-1</sup>. The rough  $\text{TiO}_2$  nanofibers are labeled as T.

$\text{TiO}_2/\text{CuInS}_2$  heterostructures were synthesized through a hydrothermal method. Typically, a transparent solution was formed by mixing 0.0125 mmol  $\text{Cu}(\text{NO}_3)_2$  (the mass ratio of  $\text{CuInS}_2$  was 1 wt. %), 0.0125 mmol  $\text{In}(\text{NO}_3)_2$  and 0.025 mmol L-cysteine hydrochloride with 80 mL deionized water. Then 0.1 g TiO<sub>2</sub> nanofibers were added to the above solution under vigorous stirring. The obtained suspension was transferred to a Teflon cup of 100 mL inner volume in a stainless steel-lined autoclave. The autoclave was maintained at 160 °C for 12 h and then was allowed to cool to room temperature. The solid product was washed with deionized water and ethanol several times and dried at 80 °C for 4 h to obtain  $\text{TiO}_2/\text{CuInS}_2$  heterostructures. For comparison,  $\text{TiO}_2/\text{CuInS}_2$  samples with various mass ratios of  $\text{CuInS}_2$  were synthesized by varying the amount of  $\text{Cu}(\text{NO}_3)_2$  from 0.03, 0.06 to 0.12 mmol while fixing the molar ratio of  $\text{Cu}(\text{NO}_3)_2 : \text{In}(\text{NO}_3)_2 : \text{L-cysteine hydrochloride}$  at 1:1:2. The nominal mass ratios of  $\text{CuInS}_2$  were 2.5 wt. %, 5 wt. % and 10 wt. %, respectively. These  $\text{TiO}_2/\text{CuInS}_2$  samples were labeled as TC<sub>x</sub> ( $x = 1, 2.5, 5, 10$ ). The actual compositions of the samples were determined by inductively coupled plasma atomic emission spectrometry (ICP-AES) by using a Prodigy 7 spectrometer (see Table 1)

**Table 1**  
Physical properties of the samples.

Samples	$\text{CuInS}_2$ (mol%)	$S_{\text{BET}}$ (m <sup>2</sup> /g)	PV (m <sup>3</sup> /g)	APS (nm)
T	–	43	0.14	10
TC1	1.4	68	0.18	10.4
TC2.5	3.1	102	0.45	17.6
TC5	5.2	83	0.45	21.5
TC10	9.4	51	0.25	20.1

PV: pore volume, APS: average pore size.

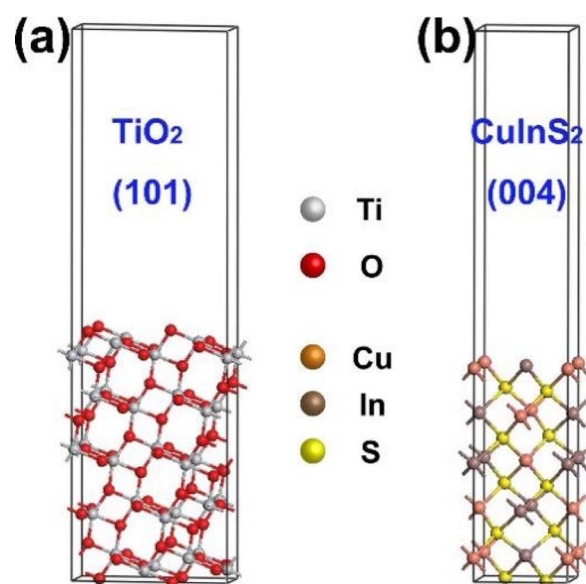


**Fig. 1.** Geometric structure of (a)  $\text{TiO}_2$  (101) surface and (b)  $\text{CuInS}_2$  (004) surface. The grey, red, orange, brown and yellow spheres stand for Ti, O, Cu, In and S atoms, respectively.

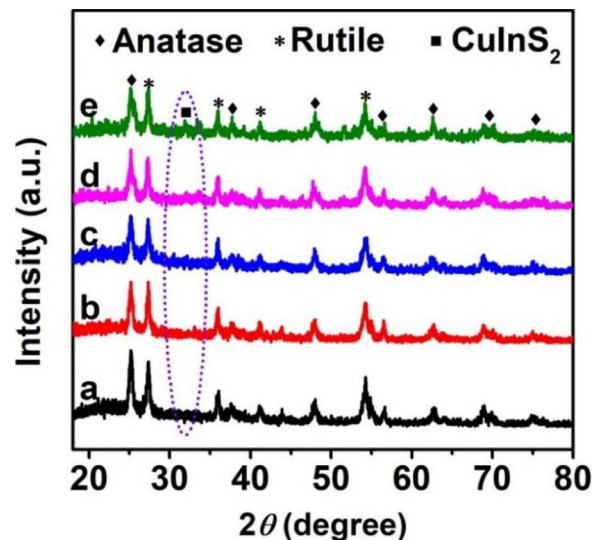


**Fig. 2.** XRD patterns of the samples: (a) T, (b) TC1, (c) TC2.5, (d) TC5 and (e) TC10. (For interpretation of the references to colour in this figure legend, the reader is referred to the web version of this article).

### 2.3. Characterization

The X-ray diffraction (XRD) patterns were recorded on a D/Max-RB X-ray diffractometer (Rigaku, Japan) with  $\text{Cu K}\alpha$  radiation ( $\lambda = 0.15418$  nm) with a scan rate ( $2\theta$ ) of 0.05° s<sup>-1</sup>. The morphology was observed on a JSM 7500F field emission scanning electron microscope (FESEM). Transmission electron microscopy (TEM) images and energy dispersive X-ray (EDX) spectrometer were recorded on a Titan G2 60–300 electron microscope. Nitrogen adsorption-desorption data were recorded on a Micromeritics ASAP 3020 nitrogen adsorption apparatus (USA) at 77 K. Prior to measurements, the samples were degassed at 150 °C for 12 h. The specific surface areas ( $S_{\text{BET}}$ ) calculated by the Brunauer-Emmett-Teller (BET) method using adsorption data in a relative pressure range from 0.05 to 0.3. The total pore volumes were estimated from nitrogen adsorption volume adsorbed at the relative pressure of 0.97. The pore size distributions were calculated from desorption data of isotherms using the Barret-Joyner-Halender (BJH)

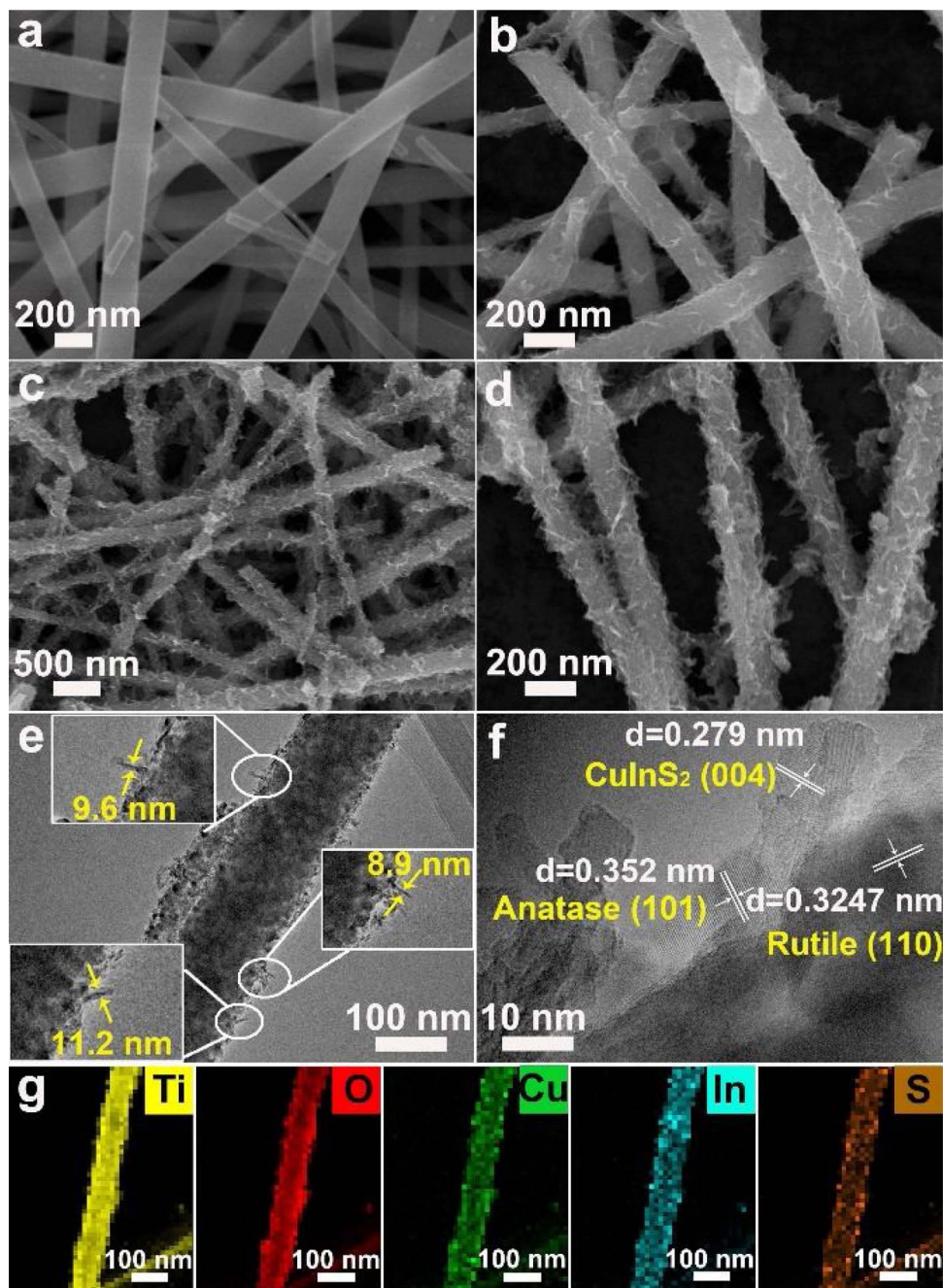


Fig. 3. SEM images of (a and b) T and (c and d) TC2.5. TEM image (e) and HRTEM image (f) of TC2.5. EDX element mappings of (g) Ti, O, Cu, In and S elements for TC2.5.

method. UV-vis diffuse reflectance spectra of samples were recorded on a Shimadzu UV-2600 UV-vis spectrophotometer (Japan) using  $\text{BaSO}_4$  as a reference. X-ray photoelectron spectroscopy (XPS) measurements were conducted on a Thermo ESCALAB 250Xi instrument with  $\text{Al K}_\alpha$  X-ray radiation. The binding energy was calibrated with reference to C 1s signal (284.8 eV).

#### 2.4. Photoelectrochemical measurements

The photoelectrochemical measurements were conducted in 0.5 M  $\text{Na}_2\text{SO}_4$  aqueous solution on a CHI660C electrochemical workstation (Shanghai CH Instruments), with a 3 W LED lamp (365 nm) as the light source. A Pt wire and saturated  $\text{Ag}/\text{AgCl}$  electrode were used as counter and reference electrodes, respectively. For preparing the working electrode, 80 mg of the photocatalysts (T, TC1, TC2.5, TC5 and TC10)

were ground with 1.0 mL ethanol to form a slurry. The slurry was blade-coated onto a 2 cm  $\times$  1.5 cm F-doped  $\text{SnO}_2$ -coated (FTO) glass with an active area of 1  $\text{cm}^2$ , followed by drying at 100 °C for 1 h. All the electrodes used had a similar thickness. The EIS measurements were carried out by applying the bias of the open circuit potential and recorded over a frequency range of 0.01–10<sup>5</sup> Hz with an ac amplitude of 10 mV.

#### 2.5. Analysis of hydroxyl radicals ( $\cdot\text{OH}$ )

A terephthalic acid (TA) fluorescence probe method was used to quantitatively analyze the production of  $\cdot\text{OH}$ . Typically, 0.1 g of photocatalyst was dispersed in a 20 mL solution containing 0.5 mM TA and 5 mM NaOH. The suspension was placed in a dish with a diameter of 9 cm. A 350 W Xe arc lamp (Zhenjian Silver Jewelry Chemical, China)

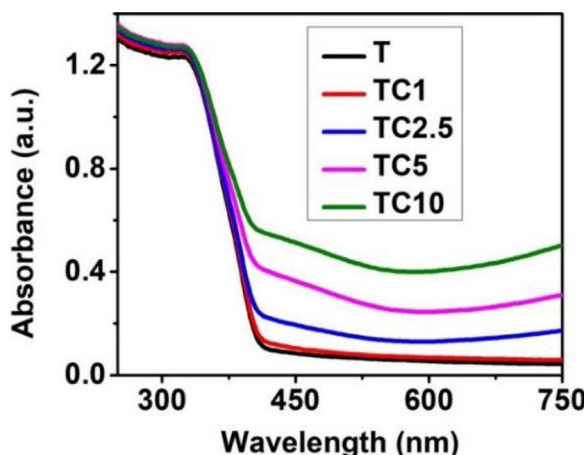


Fig. 4. Diffuse reflectance spectra of the samples.

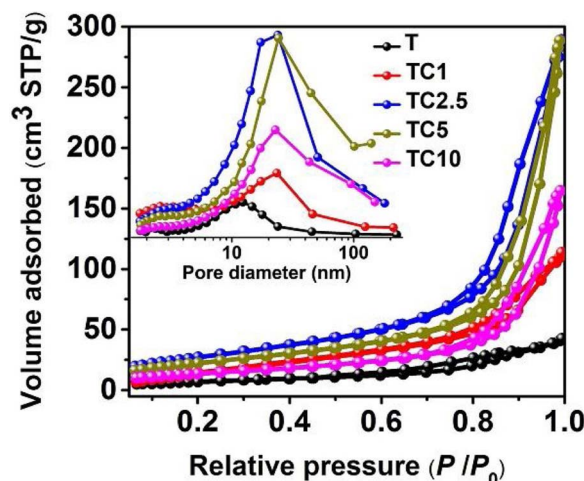


Fig. 5. Left: nitrogen adsorption-desorption isotherms (inset: pore size distributions) of the samples. Right (Table 1): specific surface area ( $S_{BET}$ ), pore volume (PV) and average pore size (APS) derived from the isotherms.

was positioned 25 cm above the dish. The light intensity on the solution was measured to be  $2.0 \text{ mW cm}^{-2}$  with a UV radiometer with the peak intensity of 365 nm (model: UV-A, Photoelectric Instrument Factory of Beijing Normal University). TA easily reacts with  $\cdot\text{OH}$  and produces a highly fluorescent 2-hydroxyterephthalic acid (TAOH). The amount of  $\cdot\text{OH}$  was determined by measured the concentration of TAOH (fluorescence peak at 425 nm with an excitation wavelength of 315 nm) using a Hitachi F-7000 fluorescence spectrophotometer after centrifugation.

## 2.6. Photocatalytic reduction of $\text{CO}_2$

The photocatalytic reduction of  $\text{CO}_2$  was carried out in a 200 mL home-made Pyrex reactor with two openings. A 350 W simulated solar Xe arc lamp was used as the light source and positioned 10 cm above the reactor. A suspension was firstly placed in the reactor by ultrasonically mixing 50 mg of the catalyst and 10 mL of deionized water. After drying at  $80^\circ\text{C}$  for 2 h, the catalyst formed a uniform film coating on the bottom of the reactor. Prior to irradiation, the reactor was purged with nitrogen for 30 min to ensure an anaerobic circumstance.  $\text{CO}_2$  together with  $\text{H}_2\text{O}$  vapor was in-situ produced through the reaction of  $\text{NaHCO}_3$  (0.12 g, introduced into the reactor before seal) and the injected  $\text{H}_2\text{SO}_4$  solution (0.25 mL, 2 M). The product (1 mL) was automatically collected at given intervals (1 h) and analyzed using a Shimadzu GC-2014C gas chromatograph (Japan) equipped with an FID detector and a methanizer. Blank experiments in the absence of  $\text{CO}_2$  or

light irradiation confirmed the  $\text{CO}_2$  and light were the key factors for the  $\text{CO}_2$  reduction. Control experiment was also performed to determine whether the carbon resource came from  $\text{CO}_2$ .

$^{13}\text{CO}_2$  isotope tracer experiment was conducted to verify the carbon source of the products by using  $^{13}\text{C}$  isotope-labelled sodium bicarbonate ( $\text{NaH}^{13}\text{CO}_3$ , Cambridge Isotope Laboratories Inc., USA) and  $\text{H}_2\text{SO}_4$  aqueous solution for the photocatalytic examinations. After 1 h of photocatalytic reaction, 500  $\mu\text{L}$  of mixed gas was taken out from the reactor and examined by a gas chromatography-mass spectrometer (GC-MS) (6980N network GC system-5975 inert mass selective detector, Agilent technologies, USA) to analyze the products.

## 2.7. Computational details

The density functional theory (DFT) calculations were performed by using the Cambridge Serial Total Energy Package (CASTEP). Generalized gradient approximation (GGA) with the Perdew-Burke-Ernzerhof (PBE) functional was utilized to describe the exchange-correlation interaction. The energy cutoff and Monkhorst-Pack k-point mesh were set to as 440 eV and  $7 \times 7 \times 1$ , respectively. During the geometry optimization, the convergence tolerance was set as  $1.0 \times 10^{-5} \text{ eV/atom}$  for energy and  $0.03 \text{ eV}/\text{\AA}$  for maximum force. For the construction of surface models, a vacuum of  $20 \text{ \AA}$  was used to eliminate interactions between periodic images. The geometric structures of  $\text{TiO}_2$  (101) surface and  $\text{CuInS}_2$  (004) surface are illustrated in Fig. 1. The work function is defined as  $\phi = E_V - E_F$ , where  $E_V$  and  $E_F$  are the electrostatic potentials of the vacuum and Fermi levels, respectively.

## 3. Results and discussion

### 3.1. Crystalline phase and morphology of materials

Fig. 2 shows the XRD patterns of the resultant samples with various loadings of  $\text{CuInS}_2$ . For the original  $\text{TiO}_2$  nanofibers, the diffraction peaks can be assigned to anatase  $\text{TiO}_2$  (JCPDS file No. 21-1272) or rutile  $\text{TiO}_2$  (JCPDS file No. 21-1276). No other diffraction peaks were observed for TC1 and TC2.5 because of the quite low loading of  $\text{CuInS}_2$ . In contrast, TC5 and TC10 which had higher loadings of  $\text{CuInS}_2$  show a new diffraction peak at around  $32.1^\circ$ , which correspond to the (004) plane of tetragonal  $\text{CuInS}_2$  (JCPDS file No. 85-1575). The results confirm the formation of  $\text{CuInS}_2$  by hydrothermal deposition, which can be further verified by TEM observation below.

The morphologies of the resultant samples were investigated by SEM and TEM. The SEM image of the pristine  $\text{TiO}_2$  before and after NaOH etching was shown in Fig. 3a and b, illustrating nanofibers with diameters around 150 nm and lengths of tens of micrometers. After the hydrothermal growth,  $\text{CuInS}_2$  nanoplates were deposited onto the  $\text{TiO}_2$  nanofibers, as shown in Fig. 3c and d. The very thin  $\text{CuInS}_2$  nanoplates had high surface area and more active sites can be exposed, which will be highly favourable for the photocatalytic reactions. The microstructure of the  $\text{TiO}_2/\text{CuInS}_2$  hybrid can be further revealed by TEM image (Fig. 3e), showing a  $\text{TiO}_2$  nanofiber coated by  $\text{CuInS}_2$  nanoplates with thickness of *ca.* 10 nm.

The crystalline phase of the hybrid material was also examined by high-resolution TEM (HRTEM). As shown in Fig. 3f, the lattice fringes with a spacing of 0.352 and 0.324 nm corresponded to the (101) plane of anatase  $\text{TiO}_2$  and (110) plane of rutile  $\text{TiO}_2$ , respectively. In addition, lattice fringes with a spacing of 0.279 nm were also observed, which was attributed to the (004) plane of  $\text{CuInS}_2$ . The HRTEM analysis further confirmed the generation of  $\text{CuInS}_2$  over the  $\text{TiO}_2$  nanofibers, agreeing with the XRD results as above. The EDX mapping (Fig. 3g) of the nanofiber indicates the co-existence of Ti, O, Cu, In and S elements, resulting from the heterostructured  $\text{TiO}_2/\text{CuInS}_2$  composite.

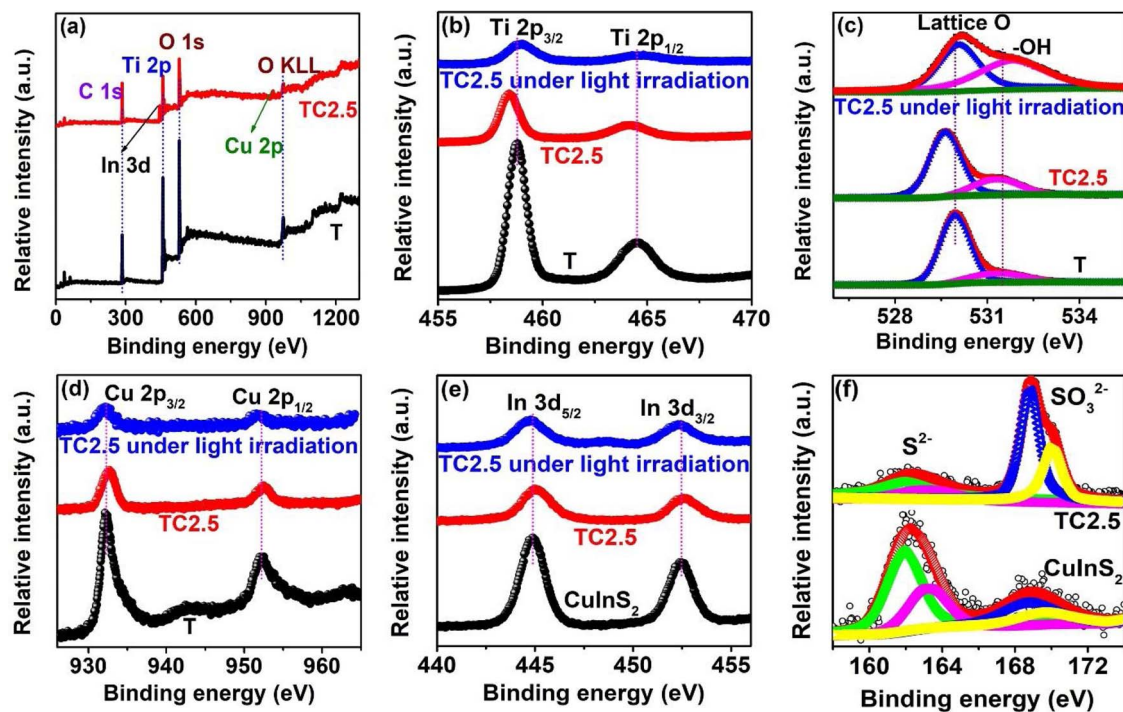


Fig. 6. (a) XPS survey spectra of T and TC2.5. XPS spectra of (b) Ti 2p and (c) O 1s of T and TC2.5. XPS spectra of (d) Cu 2p, (e) In 3d and (f) S 2p of CuInS<sub>2</sub> and TC2.5.

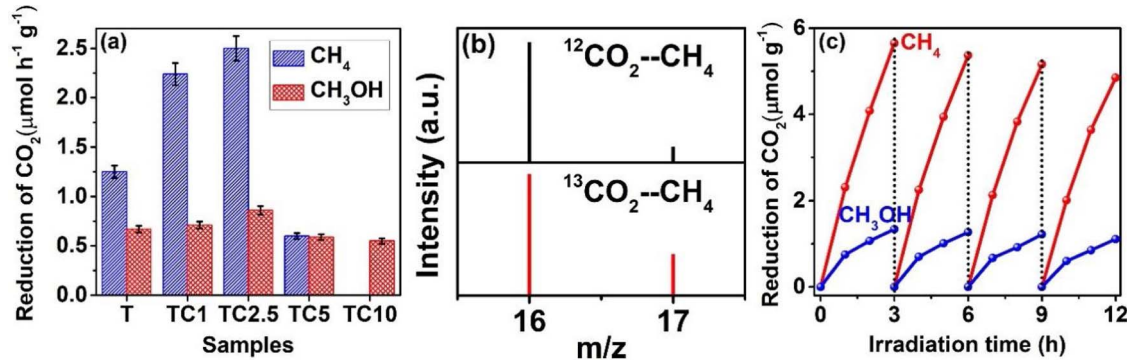


Fig. 7. (a) Photocatalytic activities of the CO<sub>2</sub> reduction over different photocatalysts. (b) The GC-MS patterns of the produced CH<sub>4</sub> over TC2.5 using <sup>12</sup>CO<sub>2</sub> and <sup>13</sup>CO<sub>2</sub> as the carbon source, respectively. (c) The long-term photocatalytic activities of TC2.5 for CO<sub>2</sub> reduction.

### 3.2. UV-vis absorption and nitrogen sorption

UV-vis diffuse reflectance spectra were measured to study the optical absorption properties of the samples, as shown in Fig. 4. As expected, the pristine TiO<sub>2</sub> sample can only absorb UV light (wavelength below 400 nm). After deposition of CuInS<sub>2</sub>, the hybrid nanofibers show enhanced visible-light absorption with the increased loading of CuInS<sub>2</sub>, resulting from the low bandgap and strong absorption capability of the CuInS<sub>2</sub> nanoplates. The significantly improved optical absorption of the hybrid can potentially result in higher photocatalytic activity for CO<sub>2</sub> reduction, as described below.

Fig. 5 shows the nitrogen adsorption-desorption isotherms and the corresponding pore size distribution curves (inset) for T, TC1, TC2.5, TC5 and TC10. All the isotherms can be identified as type IV according to the BDDT (Brunauer, Deming, Deming and Teller) classification and having H3-type hysteresis loops at  $P/P_0$  between 0.45 and 0.9, indicating the presence of narrow slit-shaped mesopores that may originate from the random distribution of CuInS<sub>2</sub> nanoplates on the TiO<sub>2</sub> nanofibers [52]. The inset of Fig. 5 shows the corresponding pore size distributions of the samples calculated according to the desorption isotherms. All the samples show mesoporous structures with the pore

size increasing from ~10 nm to ~20 nm after the coating of to the CuInS<sub>2</sub> nanoplates. Table 1 summarizes the specific surface areas ( $S_{\text{BET}}$ ), pore volumes and pore sizes of the samples. The  $S_{\text{BET}}$  of the samples shows a volcano shape and reaches the maximum value of 102 m<sup>2</sup> g<sup>-1</sup> for TC2.5, as the loading of CuInS<sub>2</sub> was increased.

### 3.3. XPS analysis

The surface composition and chemical states of the resultant samples were investigated by XPS. The survey XPS spectrum (Fig. 6a) shows the presence of Cu and In elements for TC2.5, in addition to Ti and O, confirming the generation of CuInS<sub>2</sub>. Fig. 6b shows the high-resolution Ti 2p spectrum with two symmetrical peaks corresponding to Ti 2p<sub>3/2</sub> at 458.8 eV and Ti 2p<sub>1/2</sub> at 464.5 eV, respectively. The O 1s XPS spectra of both samples (Fig. 6c) can be deconvoluted to lattice oxygen (529.8 eV) in TiO<sub>2</sub> and –OH species (531.6 eV). Note that the binding energies of both Ti 2p and O 1s for TC2.5 shifted by 0.5 eV to lower values as compared to T, suggesting the presence of electron transfer from CuInS<sub>2</sub> to TiO<sub>2</sub> after hybridization, which will build an internal electric field at the interface of the hybrid. The directed electron transfer between the two components of the hybrid can be further

**Table 2**  
Photocatalytic CO<sub>2</sub> reduction performances of various TiO<sub>2</sub>-based photocatalysts.

Photocatalyst	Reducant	Light	Product	Yield ( $\mu\text{mol g}^{-1} \text{h}^{-1}$ )	Ref.
2.5 % CuInS <sub>2</sub> /TiO <sub>2</sub>	H <sub>2</sub> O vapor	350 W Xe lamp	CH <sub>4</sub>	2.5	This work
CuIn <sub>2</sub> S <sub>4</sub> -0.33/TiO <sub>2</sub>	H <sub>2</sub> O vapor	300 W Xe lamp	CH <sub>3</sub> OH	0.86	[53]
Pt/TiO <sub>2</sub>	H <sub>2</sub> O vapor	300 W Xe lamp	CH <sub>4</sub>	4.8	[54]
1.5 % Ag/TiO <sub>2</sub>	H <sub>2</sub> O vapor	300 W Xe lamp	CO	0.1	[55]
Pt-Cu <sub>2</sub> O/TiO <sub>2</sub>	H <sub>2</sub> O vapor	300 W Xe lamp	CH <sub>4</sub>	1.42	[56]
Ag-Mn-N/TiO <sub>2</sub>	H <sub>2</sub> O vapor	300 W Xe arc lamp	CO	0.05	[26]
5 wt.% GO/TiO <sub>2</sub>	H <sub>2</sub> O vapor	500 W Xe arc lamp	CH <sub>4</sub>	0.5	[17]
			CO	1.86	
			C <sub>2</sub> H <sub>6</sub>	0.05	
			C <sub>2</sub> H <sub>4</sub>	0.51	
A/R-TiO <sub>2</sub>	H <sub>2</sub> O vapor	100 W Xe lamp	CH <sub>4</sub>	1.13	[57]
TiO <sub>2</sub> flakes	H <sub>2</sub> O liquid	300 W Hg lamp	Formate	1.9	[58]

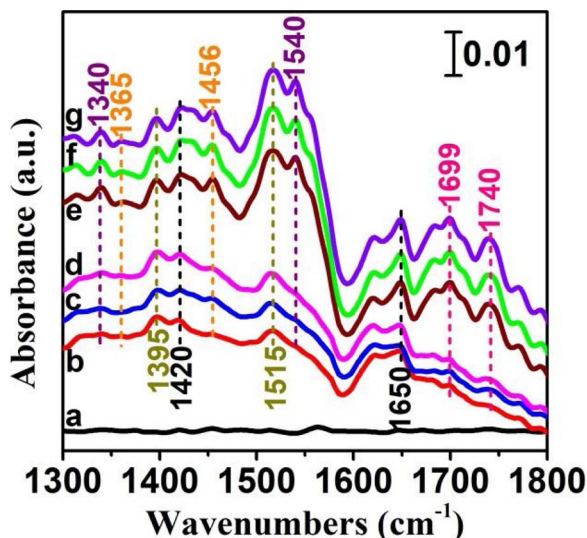


Fig. 8. *In-situ* DRIFTS spectra of TC2.5 under the flow CO<sub>2</sub>/H<sub>2</sub>O: (a) in the absence of CO<sub>2</sub>/H<sub>2</sub>O in the dark, (b–d) after the introduction of CO<sub>2</sub>/H<sub>2</sub>O for 20, 40 and 60 min in the dark, and (e–g) after the photo-irradiation for 20, 40 and 60 min.

verified by the DFT calculation shown below. The electron transfer and the associated electric field would play a role in the heterojunction formation and hence affect the photocatalytic activities for CO<sub>2</sub> reduction.

The Cu 2p XPS spectrum of TC2.5 shown in Fig. 6d contained two signals at 932.0 and 951.5 eV, corresponding to Cu 2p<sub>3/2</sub> and Cu 2p<sub>1/2</sub>, respectively. The two strong photoelectron signals at 444.8 and 452.3 eV in the In 3d XPS spectrum (Fig. 6e) of TC2.5 were assigned to In 3d<sub>5/2</sub> and In 3d<sub>3/2</sub>, respectively. For comparison, the XPS of pure CuInS<sub>2</sub> were also measured and shown in Fig. 6d–f. The binding energies of Cu and In for TC2.5 showed clear shift to higher values compared to those of CuInS<sub>2</sub>, implying the electron transfer from CuInS<sub>2</sub> to TiO<sub>2</sub>, which agree with the above analysis and suggest the formation of built-in electric field and direct Z-scheme heterojunction between them, as detailed below. Fig. 6f shows the XPS signal of sulfur, which can be assigned to the presence of S<sup>2–</sup> and SO<sub>3</sub><sup>2–</sup> species.

Apparently, S<sup>2–</sup> derived from the formation of CuInS<sub>2</sub>, and SO<sub>3</sub><sup>2–</sup> may be generated during the disproportionation of L-cysteine hydrochloride. The results further prove the existence of CuInS<sub>2</sub> in TC2.5, which are in good agreement with the XRD and HRTEM analyses.

### 3.4. Photocatalytic CO<sub>2</sub> reduction and *in-situ* DRIFTS measurement

For the photocatalytic CO<sub>2</sub> reduction tests, control experiments were first conducted in the absence of photocatalysts, carbon source, irradiation or H<sub>2</sub>O (N<sub>2</sub> was used as the reference gas). We found that hydrocarbons were produced only in the presence of the photocatalysts, irradiation, H<sub>2</sub>O and CO<sub>2</sub>, which verified that the hydrocarbons resulted exclusively from the photoreduction of CO<sub>2</sub>. Here, CO<sub>2</sub> can be reduced to CH<sub>4</sub> and CH<sub>3</sub>OH upon the as-prepared materials under Xe lamp irradiation. Fig. 7a shows the yields of CH<sub>4</sub> and CH<sub>3</sub>OH after 1 h of irradiation over the samples. It can be seen that the hydrocarbon yield increased with the loading of CuInS<sub>2</sub> and reached a maximum value over TC2.5, with the production rate of 2.5  $\mu\text{mol h}^{-1} \text{g}^{-1}$  for CH<sub>4</sub> and 0.86  $\mu\text{mol h}^{-1} \text{g}^{-1}$  for CH<sub>3</sub>OH. We consider the improvements resulted from the enhanced light absorption, increased surface area and possible improved charge separation and extraction after the growth of CuInS<sub>2</sub>. We note that the generation rate of CH<sub>4</sub> by TC2.5 almost doubled the generation rate by T, while the yield of CH<sub>3</sub>OH only showed a minor increase. Further rising of the CuInS<sub>2</sub> amount would result in a decrease of photocatalytic efficiency (sample TC5 and TC10).

We note that the product (CH<sub>4</sub> and CH<sub>3</sub>OH) distribution of CO<sub>2</sub> reduction over TiO<sub>2</sub>/CuInS<sub>2</sub> varied with the loading amount of CuInS<sub>2</sub>. From the thermodynamic point of view, the reduction potential of CO<sub>2</sub> → CH<sub>4</sub> (−0.24 V vs. NHE, pH7) is more positive than that of CO<sub>2</sub> → CH<sub>3</sub>OH<sub>4</sub> (−0.38 V vs. NHE, pH7). We speculate that with increasing amount of CuInS<sub>2</sub>, more electrons can be generated and/or transferred to react with CO<sub>2</sub> molecules. Meanwhile, since the CO<sub>2</sub> → CH<sub>4</sub> is energetically more favourable than CO<sub>2</sub> → CH<sub>3</sub>OH<sub>4</sub> as mentioned above, the CH<sub>4</sub> generation rate was improved with the loading of CuInS<sub>2</sub>, and meanwhile the generation rate of CH<sub>3</sub>OH remained unchanged.

Further, to verify the real carbon source of the photocatalytic products, isotope tracer experiment involving photo-reduction of <sup>13</sup>CO<sub>2</sub> (<sup>12</sup>CO<sub>2</sub> was also tested as a reference) was conducted and examined by GC-MS. As shown in Fig. 7b, a strong peak assigned to <sup>13</sup>CH<sub>4</sub> (*m/z* = 17) was clearly observed when using <sup>13</sup>CO<sub>2</sub> as the carbon source, while the corresponding peak using <sup>12</sup>CO<sub>2</sub> as the carbon source was much weaker. These results confirmed that the detected products over the as-prepared photocatalyst originated from the CO<sub>2</sub> source gas rather than any residual/contaminant carbon species.

Table 2 shows the photocatalytic CO<sub>2</sub> reduction performance of various TiO<sub>2</sub>-based photocatalysts. It can be found that the TiO<sub>2</sub>/CuInS<sub>2</sub> hybrid exhibits higher or comparable photocatalytic CO<sub>2</sub> conversion activities compared with most of the recently reported TiO<sub>2</sub>-based photocatalysts. There are few materials showing higher CO<sub>2</sub> reduction efficiency, nevertheless, these photocatalysts were modified with noble metals such as Pt and Ag, which increased the cost and limited the large-scale usage. Further, the long-term stability of the TiO<sub>2</sub>/CuInS<sub>2</sub> hybrid was checked and we found that the photocatalytic CO<sub>2</sub> reduction rate was largely remained after 12 h illumination (Fig. 7c). Therefore, the easily-prepared, noble-metal-free cocatalyst of CuInS<sub>2</sub> can still be of great interest for achieving high-efficiency CO<sub>2</sub> reduction.

Further, we conducted *in-situ* DRIFTS measurement to explore the CO<sub>2</sub> photoreduction mechanism over TC2.5. As shown in Fig. 8, no absorption bands can be found in the absence of CO<sub>2</sub> and H<sub>2</sub>O (Fig. 8a) in the dark. When CO<sub>2</sub> and water vapor were introduced into the reactor for 20 min in the dark, the molecules can be adsorbed onto TC2.5, evidenced by the presence of the monodentate bicarbonate species at 1650  $\text{cm}^{-1}$  ( $\nu_{\text{as}}(\text{CO}_3)$ ) and 1420  $\text{cm}^{-1}$  ( $\nu_{\text{s}}(\text{CO}_3)$ ) as well as bidentate bicarbonate species at 1515  $\text{cm}^{-1}$  ( $\nu_{\text{as}}(\text{CO}_3)$ ) and 1395  $\text{cm}^{-1}$  ( $\nu_{\text{s}}(\text{CO}_3)$ ) [59–61] (Fig. 8b). The absorption spectra showed no changes when the

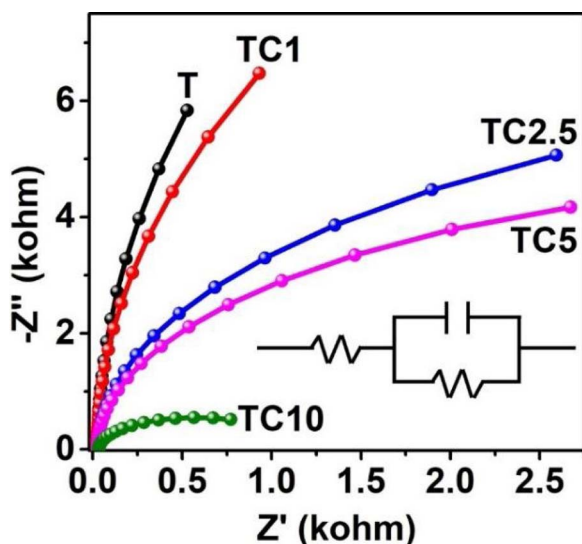


Fig. 9. Nyquist plots of the samples measured in 0.5 M  $\text{Na}_2\text{SO}_4$  aqueous solution under Xe lamp irradiation.

exposure time was further increased to 40 and 60 min (Fig. 8c and d) without illumination. Under the photoirradiation, the intensities of monodentate and bidentate bicarbonate species increase with irradiation time (Fig. 8e–g) due to the large thermodynamic tendency for the conversion of  $\text{CO}_2\text{--CO}_3^{2-}$ . Meanwhile, some new absorption bands appear at 1540 and 1340  $\text{cm}^{-1}$ , which are attributed to  $\nu_{\text{as}}(\text{CO}_2)$  and  $\nu_{\text{s}}(\text{CO}_2)$  of bidentate formic acid species [59]. The absorption bands located at 1456 and 1365  $\text{cm}^{-1}$  are assigned to  $\nu_{\text{as}}(\text{COO})$  and  $\nu_{\text{s}}(\text{COO})$  of absorbed formic acid species [60]. The bands at 1699 and 1740  $\text{cm}^{-1}$  can be ascribed to  $\nu_{\text{as}}(\text{CO})$  of absorbed formate and formic acid species, respectively [61]. It can be concluded that formate and formic acid were generated as the intermediates on the surface of  $\text{TiO}_2/\text{CuInS}_2$  nanohybrids during the  $\text{CO}_2$  reduction.

### 3.5. EIS measurement, EPR analysis and DFT calculation

Electrochemical impedance spectra (EIS) were measured to investigate the photogenerated charge transfer dynamics. Fig. 9 shows the EIS spectra of the samples and the semicircles observed in the Nyquist plots correspond to the charge transfer resistance in the sample/electrode interface. In general, a smaller semicircle implies a better charge transfer across this interface. As can be seen, the semicircle

became smaller as the content of  $\text{CuInS}_2$  was increased, indicating that the hybridization with  $\text{CuInS}_2$  was able to improve the electron transfer which thus led to a significant photocatalytic enhancement for the  $\text{CO}_2$  reduction.

Moreover, terephthalic acid (TA) was used as a probe molecule to examine the  $\cdot\text{OH}$  free radicals produced over the samples under illumination. The  $\cdot\text{OH}$  radicals can easily react with TA to produce a luminescent TAOH adduct, with fluorescence emission centered at 425 nm. Hence, the corresponding photoluminescence (PL) spectra recorded after UV illumination for different time (0–60 min) over TC2.5 were recorded and shown in Fig. 10a. The PL intensity boosted with increasing irradiation time, implying the continuous generation of hydroxyl radicals upon TC2.5 under illumination. Fig. 10b shows the time courses of the PL intensity from TAOH for different samples. Clearly, TC2.5 generated the highest amount of  $\cdot\text{OH}$  as compared to other samples and in contrast, while T showed minor PL increase even after 60 min illumination. Based on these results, we proposed a direct Z-scheme heterojunction formed between  $\text{TiO}_2$  and  $\text{CuInS}_2$ , i.e. the photo-generated electrons in the conduction band of  $\text{TiO}_2$  can transfer to the valence band of  $\text{CuInS}_2$ , reducing the recombination rate of electron/hole pairs and facilitating the production of  $\cdot\text{OH}$  in aqueous solution. In the process of  $\text{CO}_2$  reduction, we suppose that the  $\cdot\text{OH}$  radicals were captured and quenched by the hydroxyl groups from  $\text{TiO}_2$  [62,63].

The Z-scheme charge transfer pathway can be more directly evidenced by in-situ XPS measurement under light irradiation. As shown in Fig. 6b and c, the binding energies of Ti 2p and O 1s for TC2.5 under irradiation shifted positively by 0.2 eV as compared to the values in dark. Accordingly, the binding energies of Cu 2p and In 3d (Fig. 6d, e) for TC2.5 showed a negative shift of ca. 0.1 eV under irradiation. Such shifts clearly confirm the presence of electron transfer from  $\text{TiO}_2$  to  $\text{CuInS}_2$  under light irradiation driven by the direct Z-scheme heterojunction, agreeing well with the above analyses.

DFT calculations further confirm the generation of the Z-scheme heterostructure between  $\text{TiO}_2$  and  $\text{CuInS}_2$ . Generally, electrons will transfer from the semiconductor with higher Fermi energy ( $E_F$ ) level to the other semiconductor with lower  $E_F$  level at the interface of two semiconductors. In our case, the  $E_F$  level of  $\text{CuInS}_2$  is higher than that of  $\text{TiO}_2$  (Fig. 11). This means the electrons can transfer from  $\text{CuInS}_2$  to  $\text{TiO}_2$  upon contact, creating a built-in electric field in the  $\text{TiO}_2/\text{CuInS}_2$  interface with the orientation from  $\text{CuInS}_2$  to  $\text{TiO}_2$  upon contact. These analyses agree well with the XPS results as discussed above, that the electrons transfer from  $\text{CuInS}_2$  to  $\text{TiO}_2$  after hybridization to form a built-in electric field resulting from the shift of binding energies of Ti 2p, O 1s, Cu 2p and In 3d.

According to the above results and discussion, we propose a

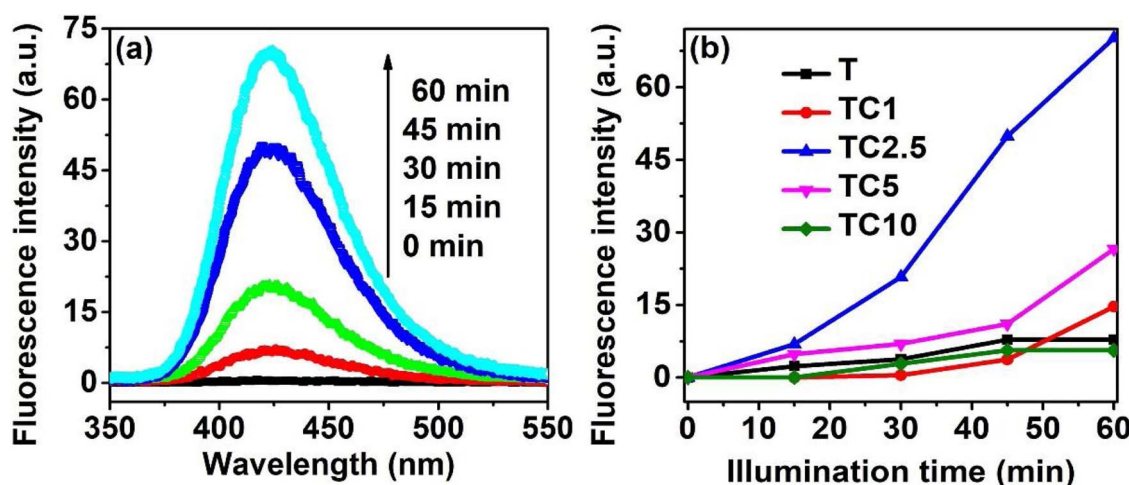


Fig. 10. (a) PL spectra of TA aqueous solution ( $5 \times 10^{-4}$  M) in the presence of TC2.5 upon illumination for 0, 15, 30, 45 and 60 min. (b) PL intensity variation (425 nm) of the TA aqueous solution against time in the presence of different samples.

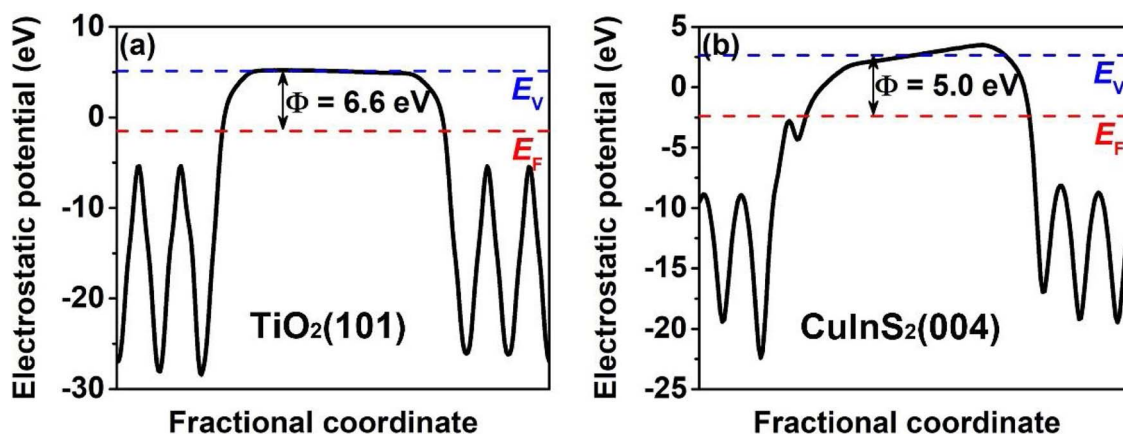


Fig. 11. Calculated electrostatic potentials for (a)  $\text{TiO}_2$  (101) face and (b)  $\text{CuInS}_2$  (004) face. The red and blue dashed lines denote Fermi level and the vacuum energy level, respectively. (For interpretation of the references to colour in this figure legend, the reader is referred to the web version of this article).

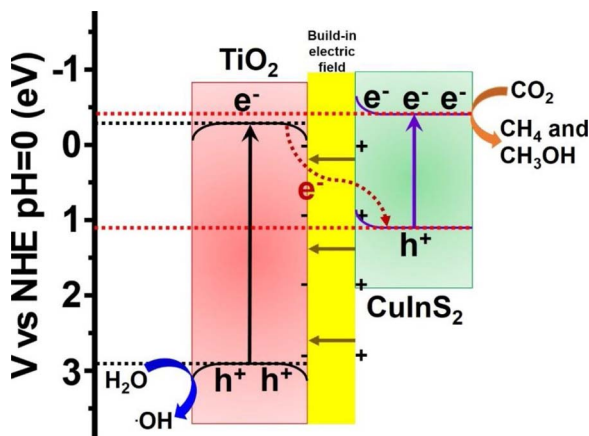


Fig. 12. Schematic illustration of the charge transfer and separation in TC2.5 under simulated sunlight light irradiation.

mechanism of the photocatalytic  $\text{CO}_2$  reduction upon the hybrid materials. Under light irradiation, the electrons in the valence band (VB) of  $\text{TiO}_2$  and  $\text{CuInS}_2$  were excited to the conduction band (CB). Owing to the presence of the internal electric field pointing from  $\text{CuInS}_2$  to  $\text{TiO}_2$ , the electrons in  $\text{TiO}_2$  CB would transfer and recombine with the holes in  $\text{CuInS}_2$  VB, instead of the electrons in  $\text{CuInS}_2$  CB transfer to  $\text{TiO}_2$  CB. This Z-scheme configuration can improve the separation and extraction of the charge carriers (electrons from  $\text{CuInS}_2$  and holes from  $\text{TiO}_2$ ) [64–66]. Therefore, the photo-induced electrons from  $\text{CuInS}_2$  CB would react with the adsorbed  $\text{CO}_2$  molecules, with the  $\text{CO}_2$  reduced to  $\text{CH}_4$  and  $\text{CH}_3\text{OH}$  with water as the proton source [67–69]. The photocatalytic mechanism and the charge transfer for the  $\text{TiO}_2/\text{CuInS}_2$  Z-scheme heterostructures are schematically illustrated in Fig. 12.

#### 4. Conclusions

In summary, novel  $\text{TiO}_2/\text{CuInS}_2$  core-shell nanofibers were fabricated through an electrospinning and subsequent hydrothermal methods. The resulting  $\text{TiO}_2/\text{CuInS}_2$  hybrid nanofibers exhibit superior photocatalytic activity for  $\text{CO}_2$  reduction under irradiation, due to the enhanced light absorption, increased surface area and most importantly, the generation of Z-scheme heterojunction between  $\text{TiO}_2$  and  $\text{CuInS}_2$ . The formation of the Z-scheme heterojunction was verified by XPS measurement, DFT calculation and free radical analysis. The direct Z-scheme heterojunction could significantly promote the charge separation and extraction upon photo-excitation, resulting in improved hydrocarbon production from  $\text{CO}_2$  reduction. Our work provides a new insight into the design and synthesis of  $\text{TiO}_2$ -based photocatalysts with

Z-scheme pathways for high-efficiency solar-fuel conversion.

#### Acknowledgements

This work was supported by NSFC (51320105001, 21573170, U1705251 and 21433007), NSFHP (2015CFA001) and Innovative Research Funds of SKLWUT (2017-ZD-4). J.X. is grateful to Discovery Early Career Researcher Award (DECRA) by Australian Research Council (DE160101488). The project is also supported by the State Key Laboratory of Advanced Technology for Materials Synthesis and Processing (Wuhan University of Technology) (2018-KF-17).

#### References

- J. Fu, J. Yu, C. Jiang, B. Cheng,  $\text{g-C}_3\text{N}_4$ -based heterostructured photocatalysts, *Adv. Energy Mater.* 8 (2018) 1701503.
- W.-H. Wang, Y. Himeda, J.T. Muckerman, G.F. Manbeck, E. Fujita,  $\text{CO}_2$  hydrogenation to formate and methanol as an alternative to photo- and electrochemical  $\text{CO}_2$  reduction, *Chem. Rev.* 115 (2015) 12936–12973.
- J. Low, J. Yu, W. Ho, Graphene-based photocatalysts for  $\text{CO}_2$  reduction to solar fuel, *J. Phys. Chem. Lett.* 6 (2015) 4244–4251.
- W. Tu, Y. Zhou, Z. Zou, Photocatalytic conversion of  $\text{CO}_2$  into renewable hydrocarbon fuels: state-of-the-art accomplishment, challenges, and prospects, *Adv. Mater.* 26 (2014) 4607–4626.
- J. Jin, T. He, Facile synthesis of  $\text{Bi}_2\text{S}_3$  nanoribbons for photocatalytic reduction of  $\text{CO}_2$  into  $\text{CH}_3\text{OH}$ , *Appl. Surf. Sci.* 394 (2017) 364–370.
- W. Yu, J. Chen, T. Shang, L. Chen, L. Gu, T. Peng, Direct Z-scheme  $\text{g-C}_3\text{N}_4/\text{WO}_3$  photocatalyst with atomically defined junction for  $\text{H}_2$  production, *Appl. Catal. B* 219 (2017) 693–704.
- T. Di, B. Zhu, B. Cheng, J. Yu, J. Xu, A direct Z-scheme  $\text{g-C}_3\text{N}_4/\text{SnS}_2$  photocatalyst with superior visible-light  $\text{CO}_2$  reduction performance, *J. Catal.* 352 (2017) 532–541.
- Y. Chen, D. Wang, X. Deng, Z. Li, Metal-organic frameworks (MOFs) for photocatalytic  $\text{CO}_2$  reduction, *Catal. Sci. Technol.* 7 (2017) 4893–4904.
- Y. Fu, D. Sun, Y. Chen, R. Huang, Z. Ding, X. Fu, Z. Li, An amine-functionalized titanium metal-organic framework photocatalyst with visible-light-induced activity for  $\text{CO}_2$  reduction, *Angew. Chem.* 51 (2012) 3364–3367.
- D. Wang, R. Huang, W. Liu, D. Sun, Z. Li, Fe-based MOFs for photocatalytic  $\text{CO}_2$  reduction: role of coordination unsaturated sites and dual excitation pathways, *ACS Catal.* 4 (2014) 4254–4260.
- F. Xu, W. Xiao, B. Cheng, J. Yu, Direct Z-scheme anatase/rutile bi-phase nanocomposite  $\text{TiO}_2$  nanofiber photocatalyst with enhanced photocatalytic  $\text{H}_2$ -production activity, *Int. J. Hydrogen Energy* 39 (2014) 15394–15402.
- J. Low, B. Cheng, J. Yu, Surface modification and enhanced photocatalytic  $\text{CO}_2$  reduction performance of  $\text{TiO}_2$ : a review, *Appl. Surf. Sci.* 392 (2017) 658–686.
- A. Nikokavoura, C. Trapalis, Alternative photocatalysts to  $\text{TiO}_2$  for the photocatalytic reduction of  $\text{CO}_2$ , *Appl. Surf. Sci.* 391 (2017) 149–174.
- J. Fu, S. Cao, J. Yu, J. Low, Y. Lei, Enhanced photocatalytic  $\text{CO}_2$ -reduction activity of electrospun mesoporous  $\text{TiO}_2$  nanofibers by solvothermal treatment, *Dalton Trans.* 43 (2014) 9158–9165.
- M. Tahir, B. Tahir, N.A.S. Amin, H. Alias, Selective photocatalytic reduction of  $\text{CO}_2$  by  $\text{H}_2/\text{O}_2$  to  $\text{CH}_4$  and  $\text{CH}_3\text{OH}$  over Cu-promoted  $\text{In}_2\text{O}_3/\text{TiO}_2$  nanocatalyst, *Appl. Surf. Sci.* 389 (2016) 46–55.
- K. Qi, B. Cheng, J. Yu, W. Ho, A review on  $\text{TiO}_2$ -based Z-scheme photocatalysts, *Chin. J. Catal.* 38 (2017) 1936–1955.
- L.-L. Tan, W.-J. Ong, S.-P. Chai, A.R. Mohamed, Photocatalytic reduction of  $\text{CO}_2$  with  $\text{H}_2\text{O}$  over graphene oxide-supported oxygen-rich  $\text{TiO}_2$  hybrid photocatalyst

under visible light irradiation: process and kinetic studies, *Chem. Eng. J.* 308 (2016) 248–255.

[18] Q. Xu, J. Yu, J. Zhang, J. Zhang, G. Liu, Cubic anatase  $\text{TiO}_2$  nanocrystals with enhanced photocatalytic  $\text{CO}_2$  reduction activity, *Chem. Commun.* 51 (2015) 7950–7953.

[19] J. Yu, J. Low, W. Xiao, P. Zhou, M. Jaroniec, Enhanced photocatalytic  $\text{CO}_2$ -reduction activity of anatase  $\text{TiO}_2$  by coexposed {001} and {101} facets, *J. Am. Chem. Soc.* 136 (2014) 8839–8842.

[20] P. Kar, S. Farsinezhad, N. Mahdi, Y. Zhang, U. Obuekwe, H. Sharma, J. Shen, N. Semagina, K. Shankar, Enhanced  $\text{CH}_4$  yield by photocatalytic  $\text{CO}_2$  reduction using  $\text{TiO}_2$  nanotube arrays grafted with Au, Ru, and Zn/Pd nanoparticles, *Nano Res.* 9 (2016) 3478–3493.

[21] O. Ola, M.M. Maroto-Valer, Synthesis, characterization and visible light photocatalytic activity of metal based  $\text{TiO}_2$  monoliths for  $\text{CO}_2$  reduction, *Chem. Eng. J.* 283 (2016) 1244–1253.

[22] M. Tahir, B. Tahir, N.A.S. Amin, Z.Y. Zakaria, Photo-induced reduction of  $\text{CO}_2$  to  $\text{CO}$  with hydrogen over plasmonic Ag-NPs/ $\text{TiO}_2$  NWs core/shell hetero-junction under UV and visible light, *J. CO<sub>2</sub> Util.* 18 (2017) 250–260.

[23] N. Umezawa, H.H. Kristoffersen, L.B. Vilhelmsen, B. Hammer, Reduction of  $\text{CO}_2$  with water on Pt-loaded rutile  $\text{TiO}_2$ (110) modeled with density functional theory, *J. Phys. Chem. C* 120 (2016) 9160–9164.

[24] Q. Wang, P. Dong, Z. Huang, X. Zhang, Synthesis of Ag or Pt nanoparticle-deposited  $\text{TiO}_2$  nanorods for the highly efficient photoreduction of  $\text{CO}_2$  to  $\text{CH}_4$ , *Chem. Phys. Lett.* 639 (2015) 11–16.

[25] W. Wang, D. Xu, B. Cheng, J. Yu, C. Jiang, Hybrid carbon@ $\text{TiO}_2$  hollow spheres with enhanced photocatalytic  $\text{CO}_2$  reduction activity, *J. Mater. Chem. A* 5 (2017) 5020–5029.

[26] M.S. Akple, J. Low, S. Liu, B. Cheng, J. Yu, W. Ho, Fabrication and enhanced  $\text{CO}_2$  reduction performance of N-self-doped  $\text{TiO}_2$  microsheet photocatalyst by bi-catalyst modification, *J. CO<sub>2</sub> Util.* 16 (2016) 442–449.

[27] V. Trevisan, A. Olivo, F. Pinna, M. Signoretto, F. Vindigni, G. Cerrato, C.L. Bianchi, C-N/ $\text{TiO}_2$  photocatalysts: effect of co-doping on the catalytic performance under visible light, *Appl. Catal. B* 160 (2014) 152–160.

[28] M.S. Akple, J. Low, Z. Qin, S. Wageh, A.A. Al-Ghamdi, J. Yu, S. Liu, Nitrogen-doped  $\text{TiO}_2$  microsheets with enhanced visible light photocatalytic activity for  $\text{CO}_2$  reduction, *Chin. J. Catal.* 36 (2015) 2127–2134.

[29] B. O'Regan, L. Xiaoe, T. Ghaddar, Dye adsorption, desorption, and distribution in mesoporous  $\text{TiO}_2$  films, and its effects on recombination losses in dye sensitized solar cells, *Energy Environ. Sci.* 5 (2012) 7203–7215.

[30] M. Wang, J. Bai, F. Le Formal, S.-J. Moon, L. Cevay-Ha, R. Humphry-Baker, C. Grätzel, S.M. Zakeeruddin, M. Grätzel, Solid-state dye-sensitized solar cells using ordered  $\text{TiO}_2$  nanorods on transparent conductive oxide as photoanodes, *J. Phys. Chem. C* 116 (2012) 3266–3273.

[31] D.O. Adekoya, M. Tahir, N.A.S. Amin, g-C<sub>3</sub>N<sub>4</sub>/(Cu/TiO<sub>2</sub>) nanocomposite for enhanced photoreduction of  $\text{CO}_2$  to  $\text{CH}_3\text{OH}$  and  $\text{HCOOH}$  under UV/visible light, *J. CO<sub>2</sub> Util.* 18 (2017) 261–274.

[32] J.E. Benedetti, D.R. Bernardo, A. Morais, J. Bettini, A.F. Nogueira, Synthesis and characterization of a quaternary nanocomposite based on  $\text{TiO}_2$ /CdS/rGO/Pt and its application in the photoreduction of  $\text{CO}_2$  to methane under visible light, *RSC Adv.* 5 (2015) 33914–33922.

[33] Y. Li, W. Zhang, X. Shen, P. Peng, L. Xiong, Y. Yu, Octahedral  $\text{Cu}_2\text{O}$ -modified  $\text{TiO}_2$  nanotube arrays for efficient photocatalytic reduction of  $\text{CO}_2$ , *Chin. J. Catal.* 36 (2015) 2229–2236.

[34] J. Liu, B. Cheng, J. Yu, A new understanding of the photocatalytic mechanism of the direct Z-scheme g-C<sub>3</sub>N<sub>4</sub>/ $\text{TiO}_2$  heterostructure, *Phys. Chem. Chem. Phys.* 18 (2016) 31175–31183.

[35] M. Reli, P. Huo, M. Sihor, N. Ambrozova, I. Troppova, L. Matejova, J. Lang, L. Svboda, P. Kustrowski, M. Ritz, P. Praus, K. Koci, Novel  $\text{TiO}_2$ /C<sub>3</sub>N<sub>4</sub> Photocatalysts for photocatalytic reduction of  $\text{CO}_2$  and for photocatalytic decomposition of  $\text{N}_2\text{O}$ , *J. Phys. Chem. A* 120 (2016) 8564–8573.

[36] A.Y. Meng, B.C. Zhu, B. Zhong, L.Y. Zhang, B. Cheng, Direct Z-scheme  $\text{TiO}_2$ /CdS hierarchical photocatalyst for enhanced photocatalytic  $\text{H}_2$ -production activity, *Appl. Surf. Sci.* 422 (2017) 518–527.

[37] H. Cao, Y. Zhu, X. Yang, C. Li, Fabrication of CuInS<sub>2</sub>- $\text{TiO}_2$  composite fibers by using electrospinning coupled with solvothermal method, *RSC Adv.* 2 (2012) 4055.

[38] S.-Z. Kang, Y.-K. Yang, W. Bu, I. Mu,  $\text{TiO}_2$  nanoparticles incorporated with CuInS<sub>2</sub> clusters: preparation and photocatalytic activity for degradation of 4-nitrophenol, *J. Solid State Chem.* 182 (2009) 2972–2976.

[39] J.-H. Yun, Y.H. Ng, S. Huang, G. Conibeer, R. Amal, Wrapping the walls of n-TiO<sub>2</sub> nanotubes with p-CuInS<sub>2</sub> nanoparticles using pulsed-electrodeposition for improved heterojunction photoelectrodes, *Chem. Commun.* 47 (2011) 11288–11290.

[40] T. Li, X. Li, Q. Zhao, Y. Shi, W. Teng, Fabrication of n-type CuInS<sub>2</sub> modified  $\text{TiO}_2$  nanotube arrays heterostructure photoelectrode with enhanced photoelectrocatalytic properties, *Appl. Catal. B* 156 (2014) 362–370.

[41] K. Guo, Z. Liu, J. Han, Z. Liu, Y. Li, B. Wang, T. Cui, C. Zhou, Hierarchical  $\text{TiO}_2$ -CuInS<sub>2</sub> core-shell nanoarrays for photoelectrochemical water splitting, *Phys. Chem. Chem. Phys.* 16 (2014) 16204–16213.

[42] T. Li, X. Li, Q. Zhao, W. Teng, Preparation of CuInS<sub>2</sub>/ $\text{TiO}_2$  nanotube heterojunction arrays electrode and investigation of its photoelectrochemical properties, *Mater. Res. Bull.* 59 (2014) 227–233.

[43] M.E. Aguirre, R.X. Zhou, A.J. Eugene, M.I. Guzman,  $\text{Cu}_2\text{O}/\text{TiO}_2$  heterostructures for  $\text{CO}_2$  reduction through a direct Z-scheme: protecting  $\text{Cu}_2\text{O}$  from photocorrosion, *Appl. Catal. B* 217 (2017) 485–493.

[44] L. Li, T.J. Daou, I. Texier, T.T. Kim Chi, N.Q. Liem, P. Reiss, Highly luminescent CuInS<sub>2</sub>/ZnS core/shell nanocrystals: cadmium-free quantum dots for in vivo imaging, *Chem. Mater.* 21 (2009) 2422–2429.

[45] I. Tsuji, H. Kato, A. Kudo, Visible-light-induced  $\text{H}_2$  evolution from an aqueous solution containing sulfide and sulfite over a ZnS-CuInS<sub>2</sub>-AgInS<sub>2</sub> solid-solution photocatalyst, *Angew. Chem.* 44 (2005) 3565–3568.

[46] Y.J. Yuan, D.Q. Chen, Y.W. Huang, Z.T. Yu, J.S. Zhong, T.T. Chen, W.G. Tu, Z.J. Guan, D.P. Cao, Z.G. Zou, MoS<sub>2</sub> nanosheet-modified CuInS<sub>2</sub> photocatalyst for visible-light-driven hydrogen production from water, *ChemSusChem* 9 (2016) 1003–1009.

[47] X. Li, K. Xie, L. Song, M. Zhao, Z. Zhang, Enhanced photocarrier separation in hierarchical graphitic-C<sub>3</sub>N<sub>4</sub>-supported CuInS<sub>2</sub> for noble-metal-free Z-scheme photocatalytic water splitting, *ACS Appl. Mater. Interfaces* 9 (2017) 24577–24583.

[48] S. Luo, J. Ke, M. Yuan, Q. Zhang, P. Xie, L. Deng, S. Wang, CuInS<sub>2</sub> quantum dots embedded in Bi<sub>2</sub>WO<sub>6</sub> nanoflowers for enhanced visible light photocatalytic removal of contaminants, *Appl. Catal. B* 221 (2018) 215–222.

[49] M. Baek, E.J. Kim, S.W. Hong, W. Kim, K. Yong, Environmentally benign synthesis of CuInS<sub>2</sub>/ZnO heteronanorods: visible light activated photocatalysis of organic pollutant/bacteria and study of its mechanism, *Photochem. Photobiol. Sci.* 16 (2017) 1792–1800.

[50] T. Xu, J. Hu, Y. Yang, W. Que, X. Yin, H. Wu, L. Chen, Ternary system of ZnO nanorods/reduced graphene oxide/CuInS<sub>2</sub> quantum dots for enhanced photocatalytic performance, *J. Alloys Compd.* 734 (2018) 196–203.

[51] J. Yuan, C. Hao, Solar-driven photoelectrochemical reduction of carbon dioxide to methanol at CuInS<sub>2</sub> thin film photocathode, *Sol. Energy Mater. Sol. Cells* 108 (2013) 170–174.

[52] K.S.W. Sing, D.H. Everett, R.A.W. Haul, L. Moscou, R.A. Pierotti, J. Rouquerol, T. Siemieniewska, Reporting physisorption data for gas/solid systems with special reference to the determination of surface area and porosity, *Pure Appl. Chem.* 57 (1985) 603–619.

[53] G. Yang, D. Chen, H. Ding, J. Feng, J.Z. Zhang, Y. Zhu, S. Hamid, D.W. Bahnemann, Well-designed 3D ZnIn<sub>2</sub>S<sub>4</sub> nanosheets/ $\text{TiO}_2$  nanobelts as direct Z-scheme photocatalysts for  $\text{CO}_2$  photoreduction into renewable hydrocarbon fuel with high efficiency, *Appl. Catal. B* 219 (2017) 611–618.

[54] Y. Wei, J. Jiao, Z. Zhao, W. Zhong, J. Li, J. Liu, G. Jiang, A. Duan, 3D ordered macroporous  $\text{TiO}_2$ -supported Pt@CdS core–shell nanoparticles: design, synthesis and efficient photocatalytic conversion of  $\text{CO}_2$  with water to methane, *J. Mater. Chem. A* 3 (2015) 11074–11085.

[55] B. Yu, Y. Zhou, P. Li, W. Tu, P. Li, L. Tang, J. Ye, Z. Zou, Photocatalytic reduction of  $\text{CO}_2$  over Ag/ $\text{TiO}_2$  nanocomposites prepared with a simple and rapid silver mirror method, *Nanoscale* 8 (2016) 11870–11874.

[56] Z. Xiong, Z. Lei, C.-C. Kuang, X. Chen, B. Gong, Y. Zhao, J. Zhang, C. Zheng, J.C.S. Wu, Selective photocatalytic reduction of  $\text{CO}_2$  into  $\text{CH}_4$  over Pt-Cu<sub>2</sub>O/ $\text{TiO}_2$  nanocrystals: the interaction between Pt and Cu<sub>2</sub>O cocatalysts, *Appl. Catal. B* 202 (2017) 695–703.

[57] A. Razzaq, S. Sinhamahapatra, T.-H. Kang, C.A. Grimes, J.-S. Yu, S.-I. In, Efficient solar light photoreduction of  $\text{CO}_2$  to hydrocarbon fuels via magnesiothermally reduced  $\text{TiO}_2$  photocatalyst, *Appl. Catal. B* 215 (2017) 28–35.

[58] S. Qamar, F. Lei, L. Liang, S. Gao, K. Liu, Y. Sun, W. Ni, Y. Xie, Ultrathin  $\text{TiO}_2$  flakes optimizing solar light driven  $\text{CO}_2$  reduction, *Nano Energy* 26 (2016) 692–698.

[59] M. Yamamoto, T. Yoshida, N. Yamamoto, T. Nomoto, Y. Yamamoto, S. Yagi, H. Yoshida, Photocatalytic reduction of  $\text{CO}_2$  with water promoted by Ag clusters in Ag/Ga<sub>2</sub>O<sub>3</sub> photocatalysts, *J. Mater. Chem. A* 3 (2015) 16810–16816.

[60] J. Szanyi, J.H. Kwon, Photo-catalytic oxidation of acetone on a  $\text{TiO}_2$  powder: an in situ FTIR investigation, *J. Mol. Catal. A Chem.* 406 (2015) 213–223.

[61] L. Liu, C. Zhao, J. Xu, Y. Li, Integrated  $\text{CO}_2$  capture and photocatalytic conversion by a hybrid adsorbent/photocatalyst material, *Appl. Catal. B* 179 (2015) 489–499.

[62] S.N. Habisreutinger, L. Schmidt-Mende, J.K. Stolarczyk, Photocatalytic reduction of  $\text{CO}_2$  on  $\text{TiO}_2$  and other semiconductors, *Angew. Chem. Int. Ed.* 52 (2013) 7372–7408.

[63] L. Liu, Y. Li, Understanding the reaction mechanism of photocatalytic reduction of  $\text{CO}_2$  with  $\text{H}_2\text{O}$  on  $\text{TiO}_2$ -based photocatalysts: a review, *Aerosol Air Qual. Res.* 14 (2014) 453–469.

[64] Y. Fu, Z. Li, Q. Liu, X. Yang, H. Tang, Construction of carbon nitride and MoS<sub>2</sub> quantum dot 2D/0D hybrid photocatalyst: direct Z-scheme mechanism for improved photocatalytic activity, *Chin. J. Catal.* 38 (2017) 2160–2170.

[65] S. Song, A. Meng, S. Jiang, B. Cheng, C. Jiang, Construction of Z-scheme Ag<sub>2</sub>CO<sub>3</sub>/N-doped graphene photocatalysts with enhanced visible-light photocatalytic activity by tuning the nitrogen species, *Appl. Surf. Sci.* 396 (2017) 1368–1374.

[66] Z. Wang, T. Hu, K. Dai, J. Zhang, C. Liang, Construction of Z-scheme Ag<sub>3</sub>PO<sub>4</sub>/Bi<sub>2</sub>WO<sub>6</sub> composite with excellent visible-light photodegradation activity for removal of organic contaminants, *Chin. J. Catal.* 38 (2017) 2021–2029.

[67] J. Low, J. Yu, M. Jaroniec, S. Wageh, A. Al-Ghamdi, Heterojunction photocatalysts, *Adv. Mater.* 29 (2017) 1601694.

[68] P. Zhou, J. Yu, M. Jaroniec, All-solid-state Z-scheme photocatalytic systems, *Adv. Mater.* 26 (2014) 4920–4935.

[69] J. Low, C. Jiang, B. Cheng, S. Wageh, A.A. Al-Ghamdi, J. Yu, A review of direct Z-scheme photocatalysts, *Small Methods* 1 (2017) 1700080.